Efficient light harvesting from flexible perovskite solar cells under indoor white light-emitting diode illumination

Citation for published version (APA):
Lucarelli, G., Di Giacomo, F., Zardetto, V., Creatore, M., & Brown, T. M. (2017). Efficient light harvesting from flexible perovskite solar cells under indoor white light-emitting diode illumination. *Nano Research*, *10*(6), 2130-2145. https://doi.org/10.1007/s12274-016-1402-5

DOI:
10.1007/s12274-016-1402-5

Document status and date:
Published: 01/06/2017

Document Version:
Typeset version in publisher’s lay-out, without final page, issue and volume numbers

Please check the document version of this publication:

• A submitted manuscript is the version of the article upon submission and before peer-review. There can be important differences between the submitted version and the official published version of record. People interested in the research are advised to contact the author for the final version of the publication, or visit the DOI to the publisher's website.
• The final author version and the galley proof are versions of the publication after peer review.
• The final published version features the final layout of the paper including the volume, issue and page numbers.

Link to publication

General rights
Copyright and moral rights for the publications made accessible in the public portal are retained by the authors and/or other copyright owners and it is a condition of accessing publications that users recognise and abide by the legal requirements associated with these rights.

- Users may download and print one copy of any publication from the public portal for the purpose of private study or research.
- You may not further distribute the material or use it for any profit-making activity or commercial gain
- You may freely distribute the URL identifying the publication in the public portal.

If the publication is distributed under the terms of Article 25fa of the Dutch Copyright Act, indicated by the “Taverne” license above, please follow below link for the End User Agreement:

www.tue.nl/taverne

Take down policy
If you believe that this document breaches copyright please contact us at:

openaccess@tue.nl

providing details and we will investigate your claim.

Download date: 08. Jul. 2024

Nano Research
DOI 10.1007/s12274-016-1402-5
Research Article

ISSN 1998-0124
CN 11-5974/O4

Efficient light harvesting from flexible perovskite solar cells under indoor white light-emitting diode illumination

Giulia Lucarelli[1], Francesco Di Giacomo[1,2], Valerio Zardetto[3], Mariadriana Creatore[3], and Thomas M. Brown[1] (✉)

[1] *Centre for Hybrid and Organic Solar Energy (CHOSE), Department of Electronic Engineering, University of Rome Tor Vergata, Via del Politecnico 1, 00133 Rome, Italy*
[2] *Holst Centre/TNO - Solliance, 5656AE Eindhoven, the Netherlands*
[3] *Department of Applied Physics, Eindhoven University of Technology, P.O. Box 513, 5600 MB Eindhoven, the Netherlands*

Received: 10 August 2016
Revised: 29 November 2016
Accepted: 2 December 2016

KEYWORDS

flexible perovskite solar cells,
indoor light harvesting,
atomic layer deposition,
nanocrystalline scaffolds,
flexible photovoltaics,
energy harvesting

ABSTRACT

This is the first report of an investigation on flexible perovskite solar cells for artificial light harvesting by using a white light-emitting diode (LED) lamp as a light source at 200 and 400 lx, values typically found in indoor environments. Flexible cells were developed using either low-temperature sol–gel or atomic-layer-deposited compact layers over conducting polyethylene terephthalate (PET) substrates, together with ultraviolet (UV)-irradiated nanoparticle TiO_2 scaffolds, a $CH_3NH_3PbI_{3-x}Cl_x$ perovskite semiconductor, and a spiro-MeOTAD hole transport layer. By guaranteeing high-quality carrier blocking (via the 10–40 nm-thick compact layer) and injection (via the nanocrystalline scaffold and perovskite layers) behavior, maximum power conversion efficiencies (PCE) and power densities of 10.8% and 7.2 $\mu W\cdot cm^{-2}$, respectively, at 200 lx, and 12.1% and 16.0 $\mu W\cdot cm^{-2}$, respectively, at 400 lx were achieved. These values are the state-of-the-art, comparable to and even exceeding those of flexible dye-sensitized solar cells under LED lighting, and significantly greater than those for flexible amorphous silicon, which are currently the main flexible photovoltaic technologies commercially considered for indoor applications. Furthermore, there are significant margins of improvement for reaching the best levels of efficiency for rigid glass-based counterparts, which we found was a high of PCE ~24% at 400 lx. With respect to rigid devices, flexibility brings the advantages of being low cost, lightweight, very thin, and conformal, which is especially important for seamless integration in indoor environments.

1 Introduction

Energy harvesting in buildings has recently attracted strong interest in the research community due to its important implications in terms of energy saving and environmental impact. The term refers to the conversion of energy sources encountered in a building, such as light, heat, and vibration, in order to power

---

Address correspondence to thomas.brown@uniroma2.it

small electronic devices such as low-power wireless autonomous sensors, which can render a building or a home “smart”. This approach entails the reduction of energy waste and consumption inside a building, while decreasing maintenance time and costs associated with the use of batteries or to the building’s power infrastructure [1]. Furthermore, the Internet of Things also requires power for enabling communications between objects [2].

Indoor photovoltaic (PV) harvesters will soon be playing a major role in supplying energy to low-operation power sensors and wireless devices, especially if PV technology can be developed and customized with these applications in mind. This is due to the widespread availability of light as an energy source inside residential and commercial buildings. In particular, demand for product-integrated photovoltaics (PIPVs), which are used to define solar cells integrated in consumer products, is rapidly growing. Indeed, PIPVs are characterized by several advantages, such as low environmental impact, autonomy and independence of operation, and convenience [3].

The design of PIPV devices for indoor applications undoubtedly represents a challenging task. This is because of the different light conditions characterizing indoor environments, owing to the different light sources used inside buildings and their variety in intensity and spectral characteristics [4]. Indoor harvesters must be optimized for specific low-illuminance conditions [5]. Apart from natural light, they must rely mainly on commonly available artificial lighting sources, including incandescent (halogen) lamps, compact fluorescent lamps, and light-emitting diodes (LEDs); it is the LEDs that are predicted to increase the share of the indoor lighting market in the future [6, 7]. The spectrum of the LED lamp used for our measurements is shown in Fig. 1. Due to the lack of an established protocol for indoor applications, the comparison of available PV technologies is not trivial. In contrast with outdoor light conditions, described in radiometric units by the reference AM1.5G spectrum of the sun and 1,000 $W \cdot m^{-2}$ (1 Sun) irradiance (see Fig. 1), indoor lighting conditions are typically defined in photometric units weighted by the sensitivity of the human eye, and are given in lux ($lx = lm \cdot m^{-2}$). Typical illuminance values in residential and commercial buildings are in the 200–1,000 lx range, which is approximately 2–3 orders of magnitude lower than 1-Sun illumination.

Different technologies have been tested under indoor conditions, such as monocrystalline and polycrystalline silicon-based devices (m-Si, poly-Si), amorphous silicon (a-Si), copper–indium–gallium–selenide (CIGS), GaAs, organic PVs (OPVs), dye-sensitized solar cells (DSSCs), and perovskite solar cells (PSCs) [8–13].

PSCs hold promise for being integrated in products, especially in their flexible form. This technology exploits the remarkable optoelectronic properties of solid-state organometal halide perovskite materials as visible to near-infrared light harvesters. Since the first report regarding PSCs [14], these devices have been extensively studied and developed because they combine low cost, ease of fabrication [15], and high efficiency [16]. Moreover, PSCs and modules [17] can be fabricated on flexible substrates [18], thus being suitable for applications where conformability, low weight, and portability are required.

In a typical metal-halide device, the perovskite active layer is sandwiched between an n-type semiconductor, usually TiO_2, as an electron-transporting material (ETM), and a solid-state hole-transporting material (HTM). 2,2′,7,7′-tetrakis-(N,N-di-p-methoxyphenyl amine)9,9′-spirobifluorene (spiro-MeOTAD) is the most common HTM [19]. This basic device architecture has been intensively investigated and modified in order to enhance PSC performance. For mesoscopic solar

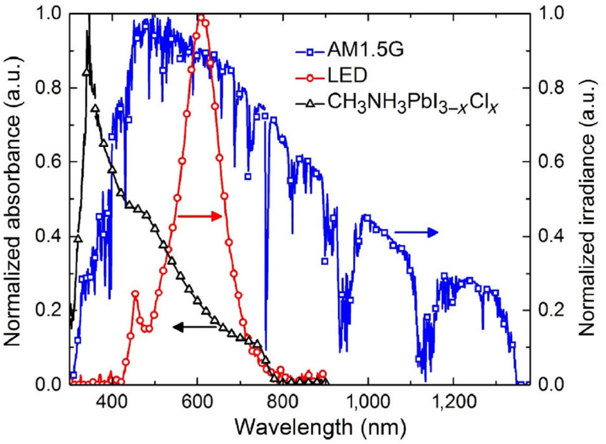

Figure 1 Normalized reference AM1.5G solar spectrum and spectral irradiance of the LED lamp used as the light source for the indoor solar cells’ characterization. The normalized absorbance spectrum of $CH_3NH_3PbI_{3-x}Cl_x$ infiltrated into a mesoporous TiO_2 layer is also reported, in order to highlight the good spectral match with the light sources.

cells, a mesoporous n-type semiconductor is deposited on top of the compact ETM layer, as a scaffold for perovskite growth, in order to enhance light harvesting and electron injection [20]. Since the organometal halide has ambipolar charge transfer characteristics, with high diffusion lengths for both electrons and holes [21], the mesoporous layer can be omitted in the device architecture, thus forming a planar PSC by maintaining just a thin compact ETM hole-blocking layer [22].

Research has extensively been conducted on PSCs with high efficiencies achieved at standard test conditions (STC, AM1.5G, 1,000 $W\cdot m^{-2}$, and 25 °C) [23–25]. However, there have been only two reports on PSCs under indoor conditions [13, 26], showing strong indoor performance on glass substrates, but none on plastic substrates. A systematic investigation carried out on PSCs on flexible substrates under these interesting conditions has not yet been explored. Flexible solar cells are particularly suited for indoor applications since they enable a more seamless integration in sensors and objects as a result of their being very thin; lightweight; conformable to even, curved surfaces; and, of course, flexible and customizable in shape. Indeed, some indoor applications on the market have already incorporated flexible DSSCs [27].

Even though much of the research has been focused on glass-based PSCs, flexible PSCs in the last few years have started to be intensively studied as reported in a recent review article [28]. The deposition of the perovskite active layer can be carried out at temperatures below 150 °C, making it compatible with the most-used plastic flexible substrates, such as polyethylene terephthalate and naphthalate (PET, PEN). Instead, low-temperature solution processing of the hole-blocking/electron-transporting compact layers constitutes a challenge for PSCs, since the most widely used materials are semiconducting oxides, such as TiO_2 and ZnO, that generally require a high-temperature treatment to enhance not only their crystallinity and electron mobility, but also their electromechanical bonding to the substrate. The first report on flexible PSCs demonstrated a device with a power conversion efficiency (PCE) of 2.6% based on a combination of electrodeposited ZnO compact layers and ZnO nanorods grown by a chemical bath [29]. Since this first report, the efficiencies of flexible PSCs based on ZnO compact layers have been boosted up to a value of 15.5% obtained with a PEN/ITO/ZnO/$CH_3NH_3PbI_3$/PTAA/Au device structure [30]; these solar cells display lower *J*–*V* hysteresis with respect to scan direction and scan rate when compared to TiO_2-based analogues, as well as excellent mechanical stability. However, devices display poor chemical stability, due to the hygroscopic and basic nature of ZnO. Replacing ZnO with TiO_2 may be a valid strategy for improving the stability of flexible PSCs. Excellent performance has also been obtained using SnO_2 [31], even reaching maximum efficiencies above 16% [32]. High efficiencies have been achieved with sputtered and electron beam-evaporated TiO_2-based flexible PSCs [33, 34]. Promising results have also been obtained with solution-processed TiO_2 compact and mesoporous layers. In particular, the first flexible module was fabricated with a screen-printed UV-irradiated TiO_2 scaffold and a TiO_2 compact layer deposited by atomic layer deposition (ALD), reaching a 3.1% PCE on a 5.6 cm × 5.6 cm PET substrate [17]. The alternative cell structure with the hole transport material at the bottom typically uses phenyl-C_{61}-butyric acid methylester as the top electron transport layer. Efficiencies of 13.4% and 14.7% have been reported using oxide (NiO_x [35]) and polymeric [36] hole-transport materials, respectively.

In this paper, we investigate the performance of flexible planar and mesoscopic $CH_3NH_3PbI_{3-x}Cl_x$-based PSCs for indoor applications on plastic substrates for the first time. Planar and mesoscopic solar cells were investigated at STC and under LED lamp illumination, at 200 and 400 lx illuminance conditions, since these are the values usually encountered in most residential environments. We show that both the compact layer and the mesoporous scaffold play a crucial role in determining the remarkable performance of our flexible PSCs, which exceeds even that of other PV technologies on flexible substrates such as a-Si and flexible DSSCs.

2 Experimental

Flexible PSCs were fabricated employing different compact and mesoporous TiO_2 (meso-TiO_2) layers. A

PET substrate coated with an indium-doped tin oxide (ITO) layer was chosen as the substrate for all of the devices. Two different device architectures were used: PET/ITO/compact TiO_2 (c-TiO_2)/$CH_3NH_3PbI_{3-x}Cl_x$/spiro-MeOTAD/Au for planar devices and PET/ITO/c-TiO_2/meso-TiO_2/$CH_3NH_3PbI_{3-x}Cl_x$/spiro-MeOTAD/Au for mesoscopic PSCs.

PET/ITO (125-μm thickness, 15 $\Omega\cdot sq^{-1}$, Flexvue) was cut with a CO_2 laser in order to obtain 2.5 cm × 2.5 cm substrates; the ITO layer was patterned by masking a 2.5-cm^2 area with a tape and etching the uncovered parts with HBr solution. The substrates were cleaned in an ultrasonic bath for 15 min in water and soap, acetone, and ethanol.

Two different kinds of TiO_2 compact layers were tested, based on solution processing and ALD techniques. The solution-processed compact layers were deposited by spin coating (2,000 rpm, 60 s) a dispersion of TiO_2 nanoparticles. The deposition parameters were optimized in order to obtain a film thickness of about 40 nm. The stable TiO_2 dispersion was obtained customizing a sol–gel (SG) method reported by Conings et al. [37]. 470 μL of titanium tetraisopropoxide was dropped in a solution of 105.4-μL HNO_3 (70 wt.%) and 2.5 mL of anhydrous ethanol; the solution was stirred for 2 h. We then added 83 μL of deionized water and 62.5 μL of acetylacetone to the solution and the dispersion was diluted with a mixture of 1-butanol:tert-butanol (1:1) to obtain a 0.127-M TiO_2 concentration. All reagents and solvents were purchased from Sigma-Aldrich.

Plasma-enhanced ALD was adopted to generate 11-nm-thick TiO_2 films at low temperatures over the PET/ITO substrates. The deposition was carried out in a thermal and remote plasma reactor (FlexAL^{TM}) by using a heteroleptic dimethylamido precursor with a methylcyclopentadienyl ligand ($Ti(CpMe)(NMe_2)_3$) and an O_2 inductively coupled plasma. The substrates underwent a plasma treatment (200 W) of 3 min before the ALD. Further details of the ALD process can be found in our previous work [17]. The thickness value for the ALD layer was measured by means of a spectroscopic ellipsometry technique. The latter measurement was carried out on a piece of silicon wafer placed in the same chamber with the ITO-PET during the ALD of the same TiO_2 layer.

The mesoporous TiO_2 layers were fabricated by spin coating two different commercial TiO_2 nanoparticle dispersions. Some devices were fabricated with a mesoporous layer obtained by spin coating (1,500 rpm, 60 s) a diluted 18-NRT paste (Dyesol, 1:5 dilution in ethanol). Other devices were fabricated with a mesoporous layer obtained by spin coating (3,000 rpm, 60 s) a TiO_2 nanoparticle dispersion in water (Sigma-Aldrich, 33 wt.%–37 wt.%). The water-based dispersion was diluted with a mixture of water and ethylene glycol (1:2 vol) in order to obtain a 7-wt.% TiO_2 concentration; 1-wt.% hydroxyethyl cellulose was added as a binder. The solvent mixture and the concentration of the water dispersion were optimized in order to overcome the poor wettability of the hydrophobic ITO layer and the resulting inhomogeneity of the deposition. We fabricated and tested devices with both formulations for the TiO_2 scaffold. The former device, formulated from the 18-NRT paste (hereafter referred to as "mesoNRT"), gave better results when combined with the atomic-layer (AL)-deposited layer, while the latter (hereafter referred to as "mesoH_2O"), formulated from the water:ethylene glycol dispersion, gave better results when combined with the SG compact layer. For the sake of clarity, we will show only these two best combinations together with the planar structures for a comparison in the main text, whereas we will also show the results with the other mesoporous layers in the Electronic Supplementary Material (ESM).

All TiO_2 mesoporous layers were thermally treated at 145 °C for 30 min and then subjected to UV irradiation for 90 min with an estimated power density of 225 $mW\cdot cm^{-2}$ (Dymax EC 5000 UV lamp with a metal-halide bulb PN38560 Dymax that contains no UV-C); this treatment is fundamental in order to promote the photo-oxidation/decomposition of the residual organic compounds in the films and to induce the coalescence of the TiO_2 nanoparticles to form a well-interconnected mesoporous structure, as already reported elsewhere [17, 38].

The mixed halide perovskite layer was deposited by means of a single-step process: CH_3NH_3I (sourced from Dyesol) and $PbCl_2$ (99%, Sigma-Aldrich) were dissolved in dimethyl formamide in order to achieve a 2.01-M CH_3NH_3I and a 0.67-M $PbCl_2$ concentration;

the active layer was deposited by spin coating (2,000 rpm, 60 s). Perovskite films were dried at room temperature for 10 min and then treated at 100 °C for 80 min. Both solution preparation and deposition of the active layer were performed in an inert atmosphere within a nitrogen-filled glove box. The hole-transporting layer was prepared by spin coating (2,000 rpm, 45 s) a doped 75 mg·mL^{-1} spiro-MeOTAD (purchased by Lumtec) solution in chlorobenzene; 8 μL of 4-tert-butylpyridine and 14.2 μL of a 520-mg·mL^{-1} $LiN(CF_3SO_2)_2N$ solution in acetonitrile were added to the spiro-MeOTAD solution. The 100-nm-thick Au cathode was deposited by thermal evaporation in a high-vacuum (10^{-6} mbar) chamber.

Current–voltage (*I*–*V*) measurements at 1 Sun (AM1.5, 100 mW·cm^{-2}) were performed using a Keithley 2420 source meter and employing a Class A solar simulator (ABET Sun 2000) as the light source.

In order to study the photovoltaic behavior in indoor conditions, a customized setup was used, as already described by De Rossi et al. [12]. A white-light LED lamp (Lexman, class A+, 62.2 lm·W^{-1} electrical-to-optical efficacy) was used as the light source for the indoor experiments and was mounted in a custom-designed box containing a height-adjustable sample holder. The irradiance spectrum of the LED lamp used in our measurements is shown in Fig. 1. The illuminance conditions were modulated at two different values, 200 and 400 lx. Further details of the experimental set-up can be found in reference [12]. Both for the indoor and outdoor characterizations, the devices were masked employing a black tape with a 0.2-cm^2 aperture.

Open-circuit voltage decay measurements were carried out using a Potentiostat/Galvanostat Autolab PGSTAT302N, by using the solar simulator as the light source; the opening and closing times of the shutter were fixed with a timer.

3 Results and discussions

3.1 Flexible perovskite solar cells with different compact and scaffold layers

Two different device architectures consisting of PET/ITO/c-TiO_2/$CH_3NH_3PbI_{3-x}Cl_x$/spiro-MeOTAD/Au and PET/ITO/c-TiO_2/meso-TiO_2/$CH_3NH_3PbI_{3-x}Cl_x$/spiro-MeOTAD/Au (with and without a mesoporous layer and with two different types of compact layers) flexible PSCs schematized in Fig. 2 were tested in order to compare the performance of the PSCs with different electron-transporting layers, both under STC (i.e., 1 Sun) and indoor illumination.

The ALD technique and the SG process were chosen to fabricate the TiO_2 compact layers. AL-deposited films are generally characterized by a low concentration of macro-defects and pinholes and the layers can be grown on flexible substrates, as the deposition can be carried out at low temperatures [17, 39, 40]. SG-processed compact layers potentially represent a good alternative to vapor-phase-grown films, because of the ease, low cost, and low temperature of the fabrication process [41].

For planar devices (Figs. 2(a) and 2(b)), the active layer was grown directly over the c-TiO_2. Typically, planar perovskite films are characterized by large grains (up to micron-sized, for fast perovskite crystallization processes [42]) and a low concentration of grain boundaries. The following morphology has been reported in the literature to provide high charge-carrier mobilities and low trap-mediated recombination rates within the perovskite layer [43]. The compact TiO_2 layer acts as selective contact by collecting photogenerated electrons through the transparent conducting oxide and preventing the recombination of these charges with the photogenerated holes at the bottom electrode [44, 45].

Mesoscopic devices (Figs. 2(c) and 2(d)) incorporate a mesoporous TiO_2 layer on top of the compact layer as a scaffold for the growth of the perovskite crystals. In this case, the dimensions of the perovskite crystals inside the scaffold are limited by the dimensions of the scaffold pores; lower mobilities are reported for small-grain perovskite films. However, high performances can be achieved for this kind of architecture; this can reasonably be ascribed to the increased contact area between the perovskite and the electron-transporting layer, as can be seen in Fig. 2, which enhances the electron injection at the bottom electrode [43] compared to planar devices with a limited contact area between the perovskite layer and the compact TiO_2 film. The scaffold can also assist in the growth

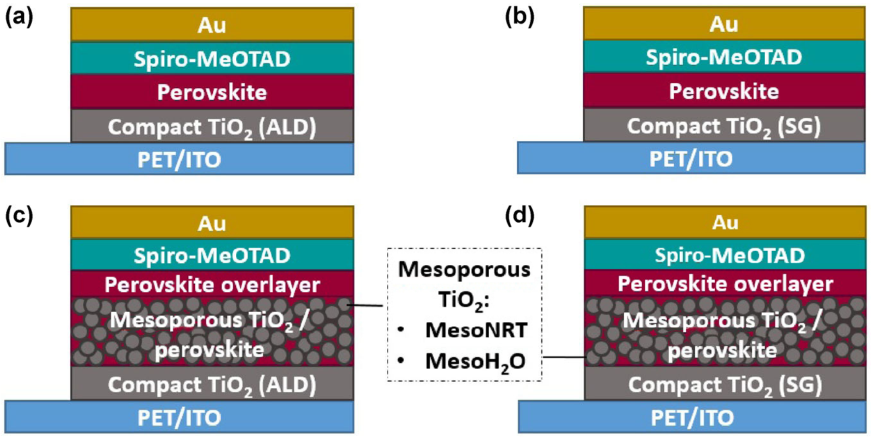

Figure 2 Flexible PSC architectures used for simulated outdoor and indoor testing. (a) and (b) For planar devices, a thin perovskite film is grown on top of a compact electron-transporting/hole-blocking layer: The compact TiO$_2$ layers investigated were obtained by means of ALD (a) or by spin coating a TiO$_2$ sol (b). In the case of mesoscopic solar cells, the perovskite layer is infiltrated in a TiO$_2$ scaffold, previously deposited on top of a compact TiO$_2$ thin film. Two different scaffolds were tested. The "mesoNRT" scaffold was deposited by spin coating an ethanol-based TiO$_2$ paste on top of the vapor phase-grown compact layer (c), while the "mesoH$_2$O" mesoporous layer was obtained by spin coating a water-based dispersion and tested in combination with the solution-processed compact layer (d).

of high-quality polycrystalline films over the scaffold. In fact, scanning electron microscopy (SEM) images of Fig. 3 show that the perovskite overlayer on top of the infiltrated mesoporous TiO$_2$ presents better-connected grains compared to that grown directly over the compact layer. We believe the large cracks appearing in the top SEM images may be ascribed to the effect of the SEM electron beam on the perovskite layer during measurement and/or the influence of the atmosphere during transport of the samples. The better interconnection of the grains can improve the electron collection properties of the layer as well as diminish the recombination probability, thus contributing to the higher performance of cells with the scaffold when compared to the planar architecture.

Furthermore, previous work has shown stability may also benefit from the presence of a scaffold, both at the glass cell level [46] and over the large-area module scale [47]. Figure 4 shows that the scaffold does indeed enhance the stability, not only of the glass-based cells, but also of our flexible devices. The shelf lives of the best-performing flexible planar (PET/ITO/ALD-TiO$_2$/CH$_3$NH$_3$PbI$_{3-x}$Cl$_x$/spiro-MeOTAD/Au) and mesoscopic (PET/ITO/ALD-TiO$_2$/meso-TiO$_2$/CH$_3$NH$_3$PbI$_{3-x}$Cl$_x$/spiro-MeOTAD/Au) cells were investigated by keeping the devices unencapsulated in the dark in a dry box (relative humidity < 15%). After one week, the planar devices showed a dramatic drop in the efficiency, mainly due to a drastic reduction of the short-circuit current. On the contrary, the mesoscopic devices displayed only a small loss in efficiency, demonstrating that scaffolds can improve the shelf life of flexible PSCs, thereby constituting one of the reasons to develop flexible PSCs incorporating a scaffold.

It is also interesting to note that the devices with the scaffold (the best-performing architecture of our set) also show very good behavior under flexibility tests. AL-deposited TiO$_2$-based mesoscopic PSCs maintained their PCE after 100 consecutive bending cycles (50 compressive + 50 tensile bending cycles) at each of 30-, 20-, and 15-mm radii of curvature [17]. With 14 mm being the limit of the safe bending radius for PET/ITO [18], it seems clear that our device stack does not entail any additional limit to the mechanical resistance of the cells, but that it is the ITO film which is currently the weakest layer for bending procedures in our device stack.

Figure 3 also presents the SEM cross-section of the PET/ITO/c-TiO$_2$/meso-TiO$_2$/CH$_3$NH$_3$PbI$_{3-x}$Cl$_x$/spiro-MeOTAD/Au flexible cell type, as well as a photograph of a solar cell with the same structure highlighting

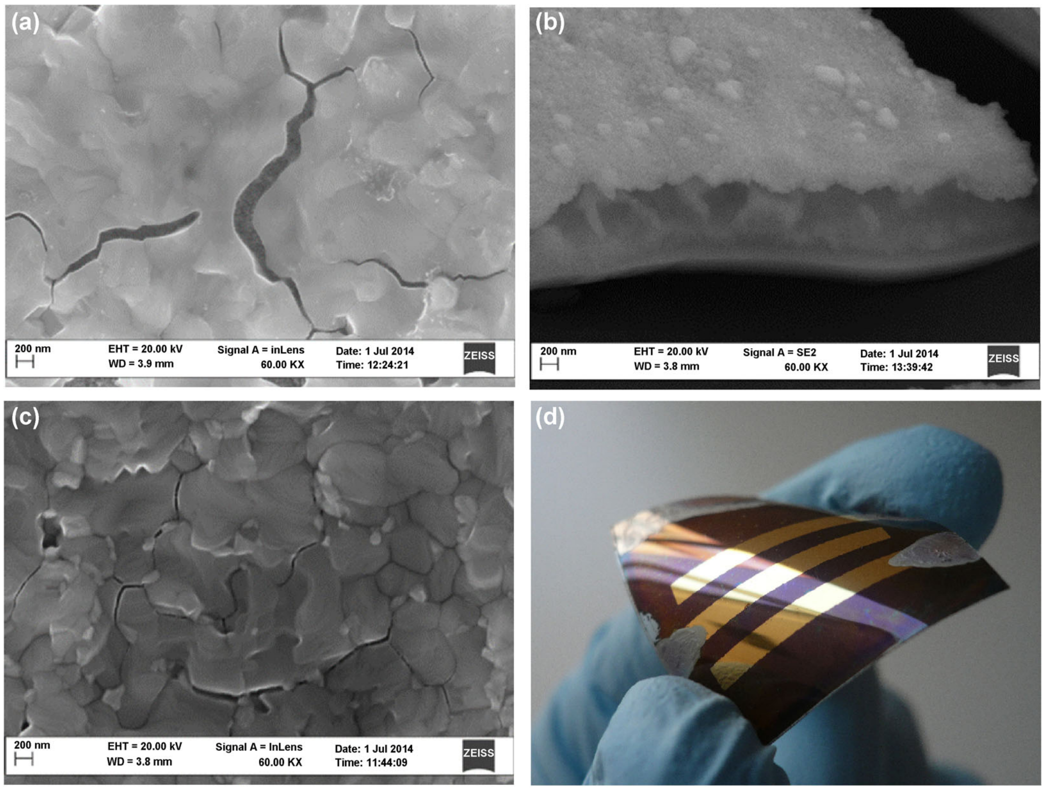

Figure 3 (a) Top-view SEM image of $CH_3NH_3PbI_{3-x}Cl_x$ grown on top of a TiO_2 scaffold in a PET/ITO/ALD-c-TiO_2; (b) cross-sectional SEM image of a PET/ITO/ALD-c-TiO_2/meso-TiO_2/$CH_3NH_3PbI_{3-x}Cl_x$ solar cell; (c) top-view SEM image of a $CH_3NH_3PbI_{3-x}Cl_x$ film grown directly on top of an ALD TiO_2 compact layer; (d) picture of a flexible PET/ITO/ALD-TiO_2/meso-TiO_2/$CH_3NH_3PbI_{3-x}Cl_x$/spiro-MeOTAD/Au solar cell.

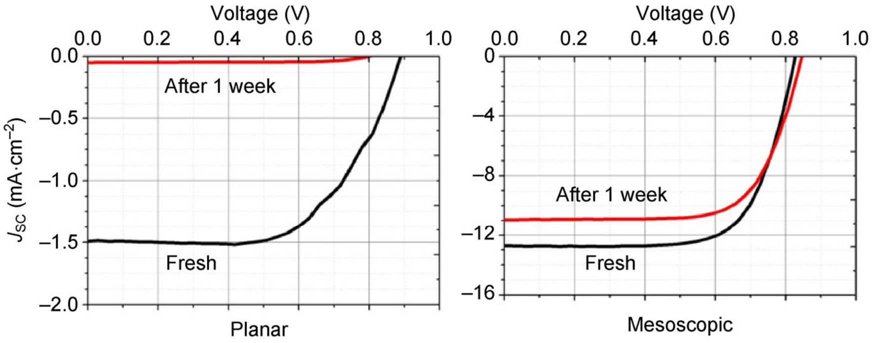

Figure 4 *J*–*V* curves of planar and mesoscopic PSCs with device architecture PET/ITO/ALD-TiO_2/$CH_3NH_3Pb_{3-x}Cl_x$/spiro-MeOTAD/Au (planar, left) and PET/ITO/ALD-TiO_2/meso-TiO_2/$CH_3NH_3PbI_{3-x}Cl_x$/spiro-MeOTAD/Au (mesoscopic, right) measured at 1 Sun. The black line represents the *J*–*V* curve of the fresh cell, while the red line is for the same device after 1 week in the dark at a relative humidity < 15%.

the nano/mesoscale dimensions of the layers and the curvability of the device.

3.2 Performance of flexible perovskite solar cells under standard test conditions

The PCEs and maximum power densities (MPDs) of the flexible planar and mesoscopic PSCs obtained at STC are shown in Fig. 5(a). The *J*–*V* curves of the best-performing devices of each structure investigated are also reported (Fig. 5(b)). Even though both compact layers were tested with each mesoporous TiO_2 layer, for simplicity, only data regarding the best-performing

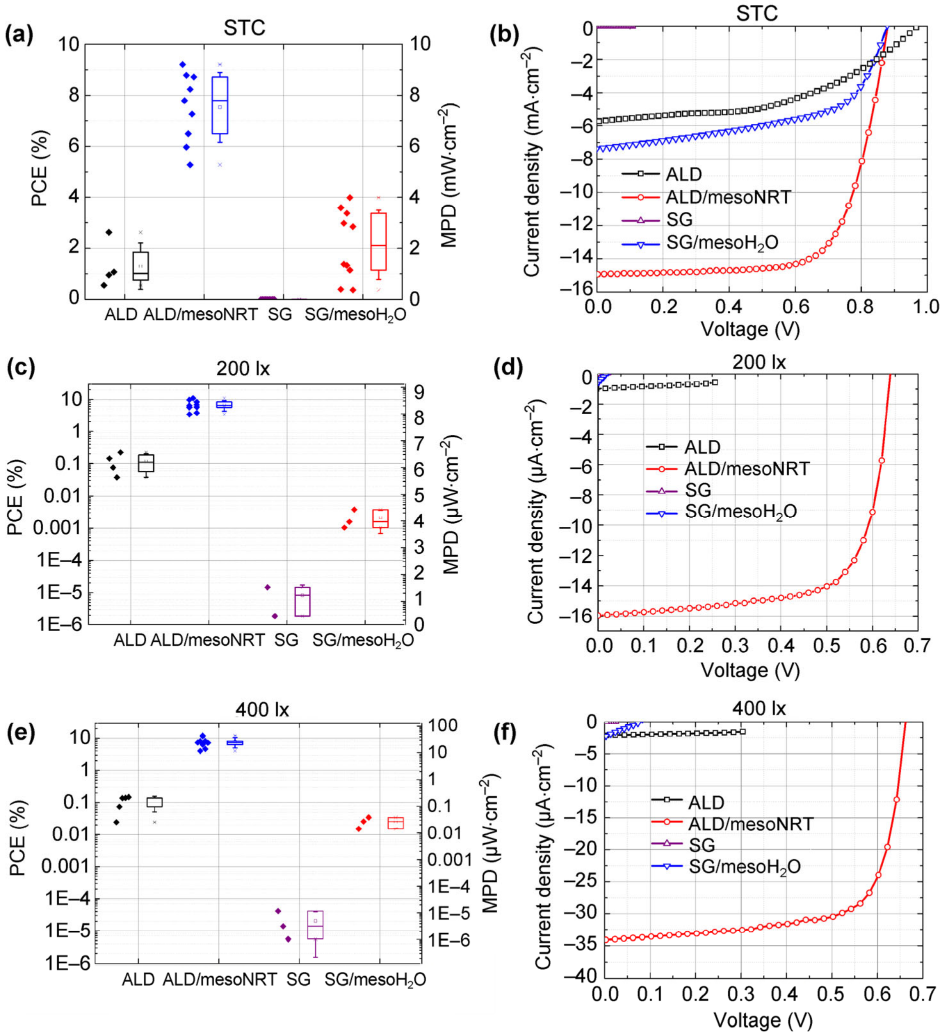

Figure 5 Power conversion efficiencies and maximum power densities of flexible PSCs measured (a) at standard testing conditions (AM1.5G, 100 mW·cm^{-2}, 25 °C; i.e., 1 Sun) and at indoor conditions under LED light at (c) 200-lx and (e) 400-lx illuminance levels. Boxes indicate the 25th and 75th percentiles and the median value, while the average value is marked with a square, the minimum and maximum values are labelled with crosses, and whiskers represent the standard deviation. *J*–*V* curves of the best-performing devices at (b) STC (i.e., 1 Sun), (d) 200 lx under LED light and (f) 400 lx under LED light.

mesoscopic cells are reported. The PV parameters (namely the PCE, the open-circuit voltage (V_{oc}), the short-circuit current density (J_{sc}), and the fill factor (FF)) of all the devices are shown in Fig. S1 in the ESM. The AL-deposited compact-layer-based planar devices with no scaffold displayed poor PCEs, mainly due to the low short-circuit current densities. This is a result of the limited charge injection at short-circuit conditions as already observed for this kind of planar device [17]. The highest PCEs for the flexible PSCs were achieved when a mesoscopic TiO_2 scaffold was added over the AL-deposited compact layer. In particular, the best performances were produced by using the ethanol-processed mesoporous mesoNRT TiO_2 layer (PCE = 9.2%, J_{sc} = 14.8 mA·cm^{-2}, V_{oc} = 0.8 V, FF = 70.1%).

A remarkable increase in the PCE with the introduction of the mesoporous scaffold can be observed, not only for the devices based on ALD, but also the SG-processed compact layers. However, the maximum efficiencies were considerably lower than those of the best-performing AL-deposited TiO_2-based solar cells for the latter type. The main cause of the lower performances of the SG-based devices is due to the poor quality of the solution-processed compact layer at these low temperatures, as will be evident later when analyzing the dark currents.

3.3 Performance of flexible perovskite solar cells under indoor LED illumination

The PCEs and MPDs at 200 and 400 lx are also reported in Figs. 5(c) and 5(e), together with those at 1 Sun. The *J*–*V* curves at 200 and 400 lx of the best-performing device of each architecture are displayed in Figs. 5(e) and 5(f). All PV parameters under indoor illumination are plotted in Figs. S2 and S3 in the ESM and are summarized in Table 1. Table 1 reports both the average and maximum PV parameters.

For indoor applications, the quality of the thin compact layer is a crucial factor in determining the overall performances of the devices, even more so than under the much more intense light at 1 Sun. Flexible solar cells based on AL-deposited compact layers and mesoporous scaffolds display high MPDs under indoor lighting conditions. The best MPD values measured for our flexible cells were 7.2 μW·cm^{-2} at 200 lx (PCE = 10.8%) and 16.0 μW·cm^{-2} at 400 lx (PCE = 12.1%), achieved with the AL-deposited compact layer and the ethanol-processed TiO_2 mesoporous scaffold. When the SG process was employed instead of the ALD for the compact layer, the MPDs and PCEs of the mesoscopic devices were reduced by two to five orders of magnitude. As previously discussed in regard to the outdoor performances of the flexible PSCs, we attribute this behavior to the poor quality of the solution-processed SG compact layer. We also note

Table 1 Average photovoltaic parameters at 200 lx, 400 lx, and AM1.5G illumination conditions for the best-performing planar and mesoscopic flexible solar cells based on two different compact layers that consist of compact TiO_2 deposited by ALD or by spin coating a TiO_2 sol. In the case of the AL-deposited compact layer, an ethanol-based TiO_2 nanoparticle dispersion was used for the mesoporous layer, while a water-based TiO_2 scaffold was employed in combination with the SG compact layer. The standard deviation is also reported. The value in squared brackets represents the maximum value obtained for each parameter

Compact layer	Device architecture	Light source	V_{oc} (mV)	J_{sc} (mA·cm^{-2})	FF (%)	PCE (%)	P_{max} indoor (μW·cm^{-2})
ALD-TiO_2	Planar	AM 1.5G	909 ± 59 (966)	–2.9 ± 1.8 (–5.5)	46.7 ± 8.8 (58.2)	1.3 ± 0.9 (2.6)	—
		LED 200 lx	181 ± 67 (236)	$(-9.1 \pm 1.1) \times 10^{-4}$ (1.0×10^{-4})	37.9 ± 14.7 (70)	0.1 ± 0.1 (0.2)	$(6.9 \pm 5.3) \times 10^{-2}$ (1.5×10^{-1})
		LED 400 lx	194 ± 71 (239)	–1.6 ± 0.2 (–1.8)	42.3 ± 14.6 (63.2)	$(1.1 \pm 0.4) \times 10^{-1}$ (1.5×10^{-1})	$(1.4 \pm 0.7) \times 10^{-1}$ (1.9)
ALD-TiO_2	Mesoscopic	AM 1.5G	861 ± 27 (893)	–12.1 ± 2.2 (–14.8)	71.9 ± 2.9 (75.3)	7.5 ± 1.4 (9.2)	—
		LED 200 lx	598 ± 42 (640)	$(-12.3 \pm 2.6) \times 10^{-3}$ (-15.8×10^{-3})	58.1 ± 16.7 (75.2)	6.7 ± 2.5 (10.8)	4.4 ± 1.7 (7.2)
		LED 400 lx	631 ± 28 (662)	$(-26.3 \pm 5.7) \times 10^{-3}$ (-33.7×10^{-3})	61.6 ± 16.4 (77.3)	7.7 ± 2.7 (12.1)	10.2 ± 3.6 (16.0)
SG TiO_2	Planar	AM 1.5G	31 ± 40 (87)	$(-6.9 \pm 9.9) \times 10^{-3}$ (-23.2×10^{-3})	28.7 ± 27.3 (70.9)	$(0.8 \pm 1.4) \times 10^{-6}$ (2.3×10^{-5})	—
		LED 200 lx	$(4 \pm 5) \times 10^{-4}$ (8×10^{-4})	$(4.9 \pm 0.1) \times 10^{-2}$ (5.0×10^{-2})	26.7 (error > 100%)	$(8.3 \pm 9.1) \times 10^{-6}$ (1.5×10^{-5})	$(5.5 \pm 6.0) \times 10^{-6}$ (9.8×10^{-6})
		LED 400 lx	$(2 \pm 1) \times 10^{-3}$ (4×10^{-3})	$(3.4 \pm 0.2) \times 10^{-2}$ (3.6×10^{-3})	29.9 ± 13.5 (44.9)	$(2.0 \pm 1.8) \times 10^{-5}$ (4.2×10^{-5})	$(2.7 \pm 2.5) \times 10^{-5}$ (5.5×10^{-5})
SG TiO_2	Mesoscopic	AM 1.5G	829 ± 65 (888)	–4.5 ± 2.6 (–7.5)	54.9 ± 3.6 (60.9)	2.1 ± 1.4 (3.9)	—
		LED 200 lx	12 ± 4 (17)	$(-3.6 \pm 1.3) \times 10^{-4}$ (-5.1×10^{-4})	29.9 ± 1.3 (30.9)	$(2.1 \pm 1.4) \times 10^{-3}$ (3.8×10^{-3})	$(1.4 \pm 0.9) \times 10^{-3}$ (2.5×10^{-3})
		LED 400 lx	52 ± 9 (63)	$(-1.8 \pm 0.5) \times 10^{-3}$ (-2.1×10^{-3})	34.9 ± 1.2 (36.3)	$(2.5 \pm 1.0) \times 10^{-2}$ (3.5×10^{-2})	$(3.3 \pm 1.3) \times 10^{-2}$ (4.6×10^{-2})

that the planar solar cells with no scaffold, already demonstrating poor performance under 1-Sun illumination, exhibited negligible efficiencies under low-level light illumination. We note that the effect of both the compact layer and the mesoporous layer on performance was greatly amplified at these low-level light conditions (lux levels are three orders of magnitude lower compared to 1-Sun illumination).

3.4 Dark currents of flexible perovskite solar cells and atomic force microscopy (AFM) images of compact layers

In order to further investigate the reasons behind the different performances of flexible solar cells, dark *J*–*V* characteristics were studied for our planar and mesoscopic best-performing devices (see Fig. 6(a)). Figure 6(b) shows a box chart of the J_{on}-to-J_{off} ratio of the flexible PSCs with the four different device architectures investigated; J_{on} is defined as the current density in dark at +1 V applied voltage, while J_{off} is the current density measured when the device is polarized at −1 V.

First, the non-rectifying characteristics of the flexible planar PSC with the solution-processed SG TiO_2 compact layer processed at low temperatures highlights that the layers do not provide a hole-blocking behavior and the consequent absence of a diode characteristic indicates that the device is not working as a solar cell, also confirmed by the absence of photovoltage at 1-Sun illumination (Fig. S1 in the ESM). The SG works better when treated at high temperature on glass (results not shown), indicating that carbon-based residual compounds that derive from the titanium precursor and catalyst remain in the film, since the low-temperature treatment of the TiO_2 layer does not allow for their complete pyrolysis. These may result in defects in the film, thus lowering the overall performances of SG TiO_2-based devices.

The planar ALD-based device instead shows a very low J_{off} current in reverse bias as a result of the optimal blocking properties due to the high energy barriers at the ITO/TiO_2 interface and high-quality films with low concentration of pinholes [48]. However, the same cell also exhibits a low forward current, indicating that electron injection and current collection from the perovskite into the contact must be improved. This improvement was indeed achieved by coating the AL-deposited layer with the mesoscopic nanoparticle TiO_2 layer. The current in the forward bias was enhanced by one order of magnitude, as is evident from Fig. 6(a), when incorporating the scaffold. The addition of the mesoscopic TiO_2 layer over the SG compact layer was also beneficial since it decreased the off current. This is likely due to the nanoparticles filling, to a certain extent, pinholes present in the SG layer. However, for the planar and mesoscopic cells incorporating the SG compact layers, the on/off ratios remained significantly lower compared to those with the AL-deposited layers, as clearly shown in Fig. 6(b). The poor on/off ratios can thus be highlighted as the main cause of the lower PCEs of the SG-based devices, both in outdoor and, greatly amplified, under indoor illumination.

Indeed, the mean PCE and V_{oc}, obtained at 1 Sun,

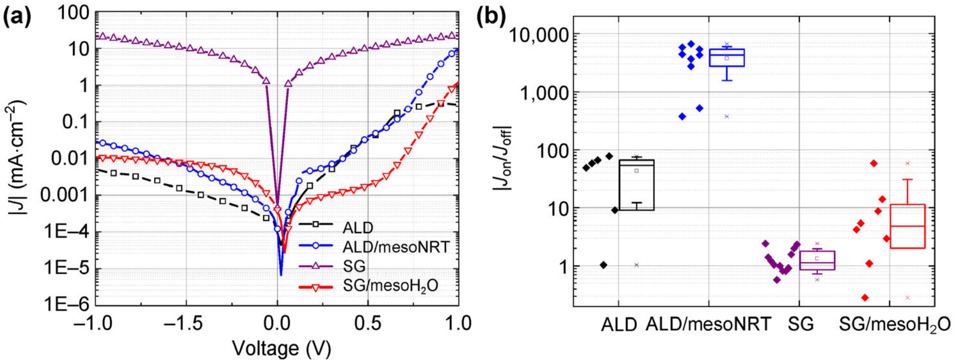

Figure 6 (a) Tafel plot of the dark current density versus voltage, measured for two planar and two mesoscopic flexible PSCs with different TiO_2 compact and mesoporous layers; (b) J_{on}/J_{off} ratio of all the flexible PSCs with the four different device architectures; J_{on} is the dark current density measured at 1 V, while J_{off} is the dark current density measured at −1 V.

for 200 and 400 lx, were plotted versus the J_{on}/J_{off} ratio average value for all of the devices studied, as displayed in Fig. 7. A clear trend linking the performance of the PSCs to their rectifying characteristics, especially at the low illumination conditions typical of an indoor environment (i.e., 200–400 lx) can be observed. In order to have efficient devices, our results, which must be statistically confirmed in the future over a larger number of device architectures and materials, seem to suggest that the J_{on}/J_{off} ratio must be greater than 10^2–10^3 at both 200 and 400 lx; otherwise the cells provide negligible power output. The analysis suggests that the power output of the flexible PSCs is strongly dependent on both the blocking and injection/transport behavior of the compact and mesoporous layer combination employed, which is much more critical when designing PSCs for indoor operation compared to that for outdoors. This result is mainly observable in the V_{oc} vs. J_{on}-to-J_{off} ratio characteristics. It is therefore obvious that the quality of the compact hole-blocking layer is a much more crucial factor for indoor than for outdoor light harvesting, as it strongly affects the performance of the flexible devices.

The AFM images of Fig. 8 assist us in clearly highlighting one of the main reasons why the AL-deposited compact layers perform so much better (especially under indoor conditions) than the SG ones in the PSCs. The AL-deposited TiO_2 layers are

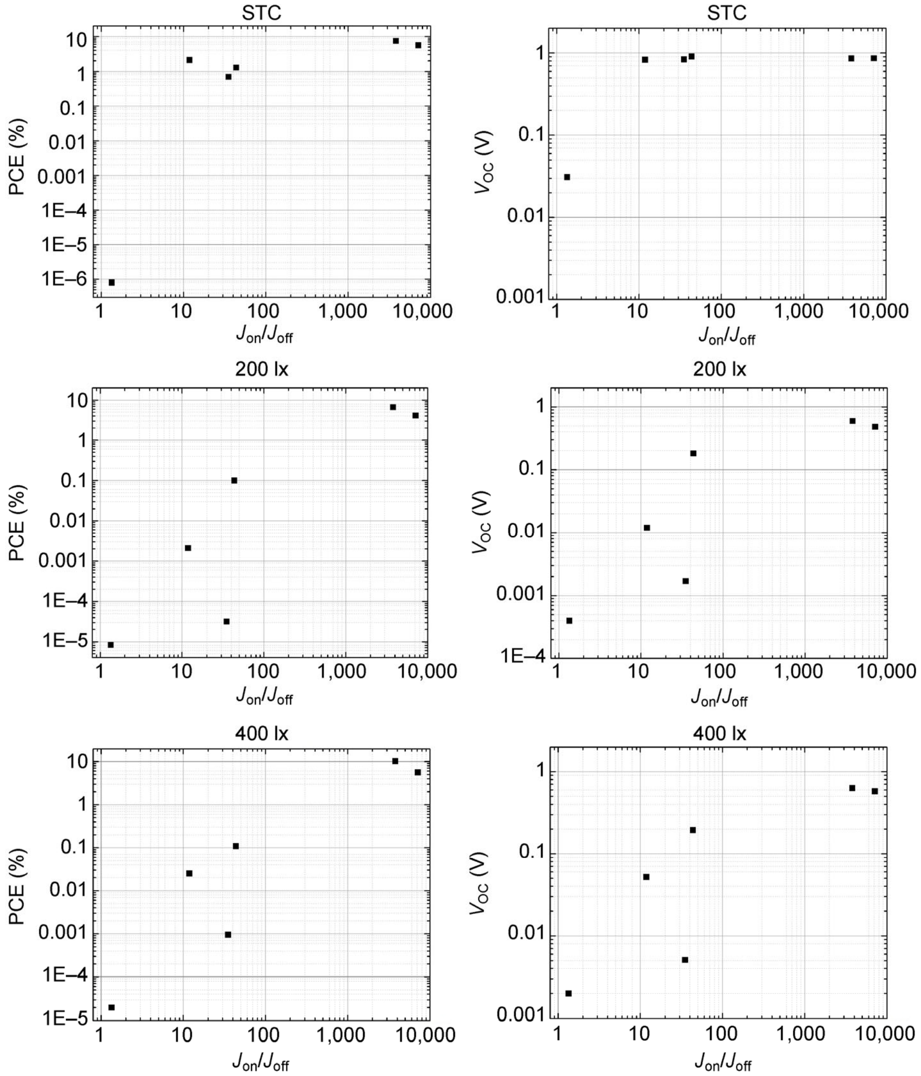

Figure 7 Average photovoltaic parameters at 200 lx, 400 lx, and STC versus average J_{on}/J_{off} ratio. V_{oc} and PCE values are reported for all the planar and mesoscopic devices fabricated in all six types used in our study.

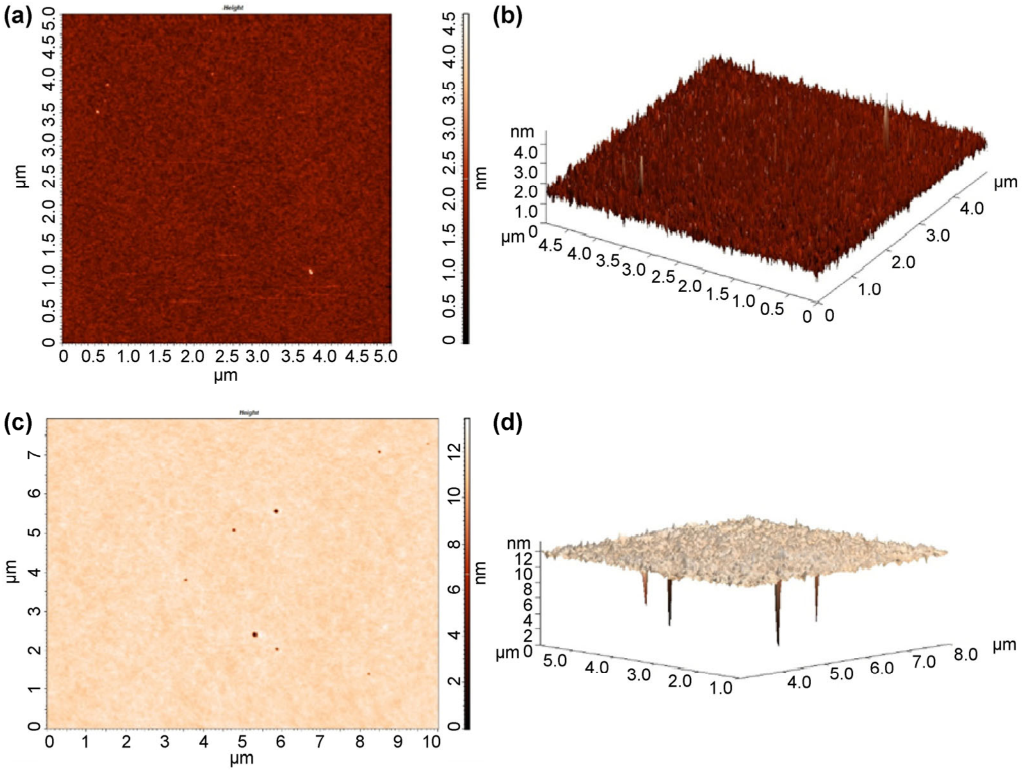

Figure 8 AFM images of TiO_2 compact layers on a silicon wafer deposited by (a) and (b) ALD and (c) and (d) by SG spin coating.

flat, uniform, and highly compact; no evident pinholes are visible from the AFM characterization. On the contrary, SG TiO_2 films clearly show deep pinholes; at least four of these are clearly visible over the 10 μm × 10 μm area. Pinholes in the "compact" layer allow for the physical contact between the perovskite layer and the ITO anode, thus enhancing the recombination of the photogenerated electrons and holes at this interface leading to a poor performance, especially at low light intensity.

In order to further gauge the differences arising from the two different compact layers, open-circuit voltage decay measurements were performed to investigate the recombination mechanisms in the flexible PSCs incorporating the mesoporous scaffold tested in this study. In particular, a comparison was made between the best-performing mesoscopic device for each of the two different compact layers; namely, the ALD/mesoNRT and SG/mesoH_2O devices. The results are shown in Fig. S4 in the ESM.

The ALD/mesoNRT solar cell displays a longer decay time, indicating a longer charge lifetime [49]. The longer decay time and the lower J_{off} of these devices (see Fig. 6) show how the AL-deposited compact layer can reduce the recombination losses at the ITO interface, improving the PV performance and enabling the use of the solar cells in indoor conditions. Furthermore, the ALD/mesoNRT solar cell exhibits a much faster rise in V_{oc}, which shows that the charges are more efficiently extracted from the perovskite with respect to the SG counterpart.

4 Discussion

The maximum power densities and associated estimated efficiencies achieved for our flexible PSCs under indoor illumination are at the very state-of-the-art, and even represent an improvement over other flexible PV technologies reported in the literature. In particular, the efficiencies are higher than for flexible a-Si and DSSCs, which are currently the main competitors to flexible perovskites for indoor applications [4, 5, 12, 50–52].

A comprehensive comparison of the performances of different technologies in indoor and outdoor conditions has been reported by De Rossi et al. [12, 51] that even includes flexible solar cells. Customized flexible DSSCs delivered 6.6 μW·cm^{-2} MPDs, at 200 lx under LED illumination [12]. Lower MPD outputs were obtained for other commercial PV technologies on flexible substrates, including a-Si [12, 51]. With our best PSC, we achieved a MPD of 7.2 μW·cm^{-2} (4.4 ± 1.7 μW·cm^{-2} average) at 200 lx and 16.0 μW·cm^{-2} (10.2 ± 3.6 μW·cm^{-2} average) at 400 lx, outperforming a-Si, flexible DSSCs, OPVs, and CIGS flexible devices at the same test conditions.

Flexible PVs are prime candidates to be utilized indoors as their properties of being thin, lightweight, and curvable make them desirable for integration in objects and surfaces, giving rise to the strong interest in this type of technology. Flexible commercial PV solar cells for indoor applications are currently available [27]. It must be noted that, as a result of less development occurring on flexible rather than rigid substrates, the efficiency of flexible PVs for all technologies lags behind that of their rigid counterparts. When also considering rigid devices, MPDs at 200 lx under LED light reported records ranging from 13.6 μW·cm^{-2} at 200 lx for glass DSSCs to 17.6 μW·cm^{-2} for expensive GaInP technology and 9.1 μW·cm^{-2} for a-Si technology [52, 53]. We have fabricated an optimized cell stack for indoor use, not only on PET substrates, but also on glass substrates (i.e., glass/ITO/ALD-TiO_2/meso-TiO_2/$CH_3NH_3PbI_{3-x}Cl_x$/spiro-MeOTAD/Au) and the average PV parameters we obtained were J_{sc} = 29.4 μA·cm^{-2}, V_{oc} = 0.63 V, FF = 71.8%, PCE = 20.2%, MPD = 13.3 μW·cm^{-2} under 200 lx LED illumination (with the best cell delivering J_{sc} = 30.8 μA·cm^{-2}, V_{oc} = 0.64 mV, FF = 72.2%, PCE = 21.3%, MPD = 14.0 μW·cm^{-2}), and J_{sc} = 59.4 μA·cm^{-2}, V_{oc} = 0.67 V, FF = 73.9%, PCE = 22.5%, MPD = 29.7 μW·cm^{-2} under 400 lx LED illumination (best cell delivering J_{sc} = 63.1 μA·cm^{-2}, V_{oc} = 0.68 mV, FF = 74.5%, PCE = 23.8%, MPD = 31.5 μW·cm^{-2}) and J_{sc} = –18.7 mA·cm^{-2}, V_{oc} = 0.88 V, FF = 72.1%, PCE = 11.9%, MPD = 11.9 mW·cm^{-2} under 1-Sun illumination (best cell delivering J_{sc} = –20.6 mA·cm^{-2}, V_{oc} = 0.90 V, FF = 74.2%, PCE = 12.9%, MPD = 12.9 mW·cm^{-2}). Thus, there is scope in closing the gap and further improving both outdoor and indoor performance, as is the case for all PV technologies. Further optimization can boost the power output. Furthermore, we have demonstrated that mesoscopic PSCs are among the top-performing solar cells, not only on rigid substrates, but also on flexible substrates where the light-harvesting performance under indoor artificial lighting is the highest reported to date, to the best of our knowledge.

5 Conclusions

Indoor energy harvesting in commercial and residential buildings via product-integrated PVs represents an important opportunity in terms of energy savings, because of the potential of powering small electronic devices. Wireless sensors and still cameras can be supplied without the use of main power or batteries, moreover allowing the communication between self-powered autonomous small devices and paving the way to the Internet of Things. Several PV technologies have been investigated and optimized for indoor applications, but no studies have so far been reported on flexible PSCs.

We investigated for the first time the performances of flexible planar and mesoscopic PSCs under artificial LED lighting, at 200 and 400 lx illuminance conditions. Different device architectures were tested, based on two different TiO_2 compact layers and two TiO_2 mesoporous scaffolds in order to find the best architecture in delivering the highest indoor performance.

We found that, both at STC and under 200- and 400-lx LED lighting, mesoscopic flexible solar cells outperformed their planar counterparts. Efficiencies as high as 10.8% (MPD = 7.2 μW·cm^{-2}) at 200 lx, 12.1% (MPD = 16.0 μW·cm^{-2}) at 400 lx, and 9.2% at STC were achieved for mesoscopic devices based on an AL-deposited TiO_2 compact layer.

On the contrary, mesoscopic devices based on a SG-deposited compact layer showed poor performance at STC and negligible power output and efficiencies in indoor conditions. Planar devices based on both compact layers displayed low efficiencies indoors and outdoors, especially because of the limited short-circuit currents.

In order to explain this behavior, we studied the rectifying characteristics. By evaluating the dark current densities in the 1 to −1 V range, it was possible to find a threshold value for the J_{on}-to-J_{off} ratio characterizing high-performance devices. These had J_{on}-to-J_{off} ratios higher than 10^3. This threshold value was achieved for mesoscopic devices fabricated with an AL-deposited TiO_2 compact layer which delivered high efficiency under indoor testing conditions.

By comparing the obtained power output of the best-performing flexible PSCs with other PV technologies for indoor applications, we highlighted the potential of PSCs for indoor energy harvesting. Indeed, our best-performing devices outperformed commercial a-Si rigid modules and, under LED lighting, are on par with or even exceed customized flexible DSSCs tested under the same conditions.

These values are still lower than rigid glass-based perovskites (PCEs of the best glass-based PSCs were 21%–24% in this study), GaInP, and DSSCs specifically designed for indoor applications. Improvements in the performance of flexible PSCs are, therefore, still required in order to ensure the future feasibility of domestic and commercial applications, by boosting the efficiencies even further, while maintaining all the intrinsic advantages of being lightweight, flexible, very thin, potentially more rugged, and conducive to a more seamless integration in the environment.

Acknowledgements

Thanks are due to Tadeo Pontecorvo and Francesca De Rossi for the indoor set-up and useful discussions. We thank MIUR for PRIN 2012 AQUASOL (2012A4Z2RY) project, "Polo Solare Organico" Regione Lazio for financial support.

Electronic Supplementary Material: Supplementary material (the photovoltaic parameters of the fabricated flexible perovskite solar cells at standard and indoor testing conditions and the open-circuit voltage rise and decay curves of the best performing devices) is available in the online version of this article at http://dx.doi.org/10.1007/10.1007/s12274-016-1402-5.

References

[1] Matiko, J. W.; Grabham N. J.; Beeby, S. P.; Tudor, M. J. Review of the application of energy harvesting in buildings. *Meas. Sci. Technol.* **2014**, *25*, 012002.

[2] Zhan, Y. Q.; Mei, Y. F.; Zheng, L. R. Materials capability and device performance in flexible electronics for the Internet of Things. *J. Mater. Chem. C* **2014**, *2*, 1220–1232.

[3] Apostolou, G.; Reinders, A.; Verwaal, M. Comparison of the indoor performance of 12 commercial PV products by a simple model. *Energy Sci. Eng.* **2016**, *4*, 69–85.

[4] Reich, N. H.; van Sark, W. G. J. H. M.; Turkenburg, W. C. Charge yield potential of indoor-operated solar cells incorporated into Product Integrated Photovoltaic (PIPV). *Renew. Energy* **2011**, *36*, 642–647.

[5] Li, Y.; Grabham, N. J.; Beeby, S. P.; Tudor, M. J. The effect of the type of illumination on the energy harvesting performance of solar cells. *Sol. Energy* **2015**, *111*, 21–29.

[6] Curtis, D. Predictions for the contribution of residential lighting to the carbon emissions of the UK to 2050. In *EEDAL Conference*, Berlin, Germany, 2009.

[7] Navigant Consulting, Inc. Energy Savings Forecast of Solid-State Lighting in General Illumination Applications; U.S. Department of Energy: Washington, DC, 2014. https://www.energy.gov/sites/prod/files/2015/05/f22/energysavingsforecast14.pdf (accessed Aug 10, 2016).

[8] Reich, N. H.; van Sark, W. G. J. H. M.; Alsema, E. A.; Lof, R. W.; Schropp, R. E. I.; Sinke, W. C.; Turkenburg, W. C. Crystalline silicon cell performance at low light intensities. *Sol. Energy Mater. Sol. Cells* **2009**, *93*, 1471–1481.

[9] Sacco, A.; Rolle, L.; Scaltrito, L.; Tresso, E.; Pirri, C. F. Characterization of photovoltaic modules for low-power indoor application. *Appl. Energy* **2013**, *102*, 1295–1302.

[10] Mathews, I.; Kelly, G.; King, P. J.; Frizzel, R. GaAs solar cells for indoor light harvesting. In *Proceedings of the 2014 IEEE 40th Photovoltaic Specialist Conference (PVSC)*, Denver, Colorado, 2014, pp 510–513.

[11] Steim, R.; Ameri, T.; Schilinsky, P.; Waldauf, C.; Dennler, G.; Scharber, M.; Brabec, C. J. Organic photovoltaics for low light applications. *Sol. Energy Mater. Sol. Cells* **2011**, *95*, 3256–3261.

[12] De Rossi, F.; Pontecorvo, T.; Brown, T. M. Characterization of photovoltaic devices for indoor light harvesting and customization of flexible dye solar cells to deliver superior efficiency under artificial lighting. *Appl. Energy* **2015**, *156*, 413–422.

[13] Chen, C.-Y.; Chang, J.-H.; Chiang, K.-M.; Lin, H.-L.; Hsiao, S.-Y.; Lin, H.-W. Perovskite photovoltaics for dim-light applications. *Adv. Funct. Mater.* **2015**, *25*, 7064–7070.

[14] Kojima, A.; Teshima, K.; Shirai, Y.; Miyasaka, T. Organometal halide perovskites as visible-light sensitizers for photovoltaic cells. *J. Am. Chem. Soc.* **2009**, *131*, 6050–6051.

[15] Razza, S.; Castro-Hermosa, S.; Di Carlo, A.; Brown, T. M. Research update: Large-area deposition, coating, printing, and processing techniques for the upscaling of perovskite solar cell technology. *APL Mater.* **2016**, *4*, 091508.

[16] Green, M. A.; Ho-Baillie, A.; Snaith, H. J. The emergence of perovskite solar cells. *Nat. Photonics* **2014**, *8*, 506–514.

[17] Di Giacomo, F.; Zardetto, V.; D'Epifanio, A.; Pescetelli, S.; Matteocci, F.; Razza, S.; Di Carlo, A.; Licoccia, S.; Kessels, W. M. M.; Creatore, M. et al. Flexible perovskite photovoltaic modules and solar cells based on atomic layer deposited compact layers and UV-irradiated TiO_2 scaffolds on plastic substrates. *Adv. Energy Mater.* **2015**, *5*, 1401808.

[18] Zardetto, V.; Brown, T. M.; Reale, A.; Di Carlo, A. Substrates for flexible electronics: A practical investigation on the electrical, film flexibility, optical, temperature, and solvent resistance properties. *J. Polym. Sci. B Polym. Phys.* **2011**, *49*, 638–648.

[19] Grätzel, M. The light and shade of perovskite solar cells. *Nat. Mater.* **2014**, *13*, 838–842.

[20] Kim, H.-S.; Lee, C.-R.; Im, J.-H.; Lee, K.-B.; Moehl, T.; Marchioro, A.; Moon, S.-J.; Humphry-Baker, R.; Yum, J.-H.; Moser, J. E. et al. Lead iodide perovskite sensitized all-solid-state submicron thin film mesoscopic solar cell with efficiency exceeding 9%. *Sci. Rep.* **2012**, *2*, 591.

[21] Stranks, S. D.; Eperon, G. E.; Grancini, G.; Menelaou, C.; Alcocer, M. J. P.; Leijtens, T.; Herz, L. M.; Petrozza, A.; Snaith, H. J. Electron–hole diffusion lengths exceeding 1 micrometer in an organometal trihalide perovskite absorber. *Science* **2013**, *342*, 341–344.

[22] Malinkiewicz, O.; Yella, A.; Lee, Y. H.; Mínguez Espallargas, G.; Grätzel, M.; Nazeeruddin, M. K.; Bolink, H. J. Perovskite solar cells employing organic charge-transport layers. *Nat. Photonics* **2014**, *8*, 128–132.

[23] Correa Baena, J. P.; Steier, L.; Tress, W.; Saliba, M.; Neutzner, S.; Matsui, T.; Giordano, F.; Jacobsson, T. J.; Srimath Kandada, A. R.; Zakeeruddin, S. M. et al. Highly efficient planar perovskite solar cells through band alignment engineering. *Energy Environ. Sci.* **2015**, *8*, 2928–2934.

[24] Saliba, M.; Matsui, T.; Seo, J.-Y.; Domanski, K.; Correa-Baena, J.-P.; Nazeeruddin, M. K.; Zakeeruddin, S. M.; Tress, W.; Abate, A.; Hagfeldt, A. et al. Cesium-containing triple cation perovskite solar cells: Improved stability, reproducibility and high efficiency. *Energy Environ. Sci.* **2016**, *9*, 1989–1997.

[25] Yang, W. S.; Noh, J. H.; Jeon, N. J.; Kim, Y. C.; Ryu, S.; Seo, J.; Seok, S. I. High-performance photovoltaic perovskite layers fabricated through intramolecular exchange. *Science* **2015**, *348*, 1234–1237.

[26] Di Giacomo, F.; Zardetto, V.; Lucarelli, G.; Cinà, L.; Di Carlo, A.; Creatore, M.; Brown, T. M. Mesoporous perovskite solar cells and the role of nanoscale compact layers for remarkable all-round high efficiency under both indoor and outdoor illumination. *Nano Energy* **2016**, *30*, 460–469.

[27] Brown, T. M.; De Rossi, F.; Di Giacomo, F.; Mincuzzi, G.; Zardetto, V.; Reale, A.; Di Carlo, A. Progress in flexible dye solar cell materials, processes and devices. *J. Mater. Chem. A* **2014**, *2*, 10788–10817.

[28] Di Giacomo, F.; Fakharuddin, A.; Jose, R.; Brown, T. M. Progress, challenges and perspectives in flexible perovskite solar cells. *Energy Environ. Sci.* **2016**, *9*, 3007–3035.

[29] Kumar, M. H.; Yantara, N.; Dharani, S.; Graetzel, M.; Mhaisalkar, S.; Boix, P. P.; Mathews, N. Flexible, low-temperature, solution processed ZnO-based perovskite solid state solar cells. *Chem. Commun.* **2013**, *49*, 11089–11091.

[30] Heo, J. H.; Lee, M. H.; Han, H. J.; Patil, B. R.; Yu, J. S.; Im, S. H. Highly efficient low temperature solution processable planar type $CH_3NH_3PbI_3$ perovskite flexible solar cells. *J. Mater. Chem. A* **2016**, *4*, 1572–1578.

[31] Park, M.; Kim, J.-Y.; Son, H. J.; Lee, C.-H.; Jang, S. S.; Ko, M. J. Low-temperature solution-processed Li-doped SnO_2 as an effective electron transporting layer for high-performance flexible and wearable perovskite solar cells. *Nano Energy* **2016**, *26*, 208–215.

[32] Wang, C. L.; Zhao, D. W.; Grice, C. R.; Liao, W. Q.; Yu, Y.; Cimaroli, A.; Shrestha, N.; Roland, P. J.; Chen, J.; Yu, Z. H. et al. Low-temperature plasma-enhanced atomic layer deposition of tin oxide electron selective layers for highly efficient planar perovskite solar cells. *J. Mater. Chem. A* **2016**, *4*, 12080–12087.

[33] Yang, D.; Yang, R. X.; Zhang, J.; Yang, Z.; Liu, S. Z.; Li, C. High efficency flexible perovskite solar cells using superior low temperature TiO_2. *Energy Environ. Sci.* **2015**, *8*, 3208–3214.

[34] Qiu, W. M.; Paetzold, U. W.; Gehlhaar, R.; Smirnov, V.; Boyen, H.-G.; Tait, J. G.; Conings, B.; Zhang, W. M.; Nielsen, C. B.; McCulloch, I. et al. An electron beam evaporated TiO_2 layer for high efficiency planar perovskite solar cells on flexible polyethylene terephthalate substrates. *J. Mater. Chem. A* **2015**, *3*, 22824–22829.

[35] Yin, X. T.; Chen, P.; Que, M. D.; Xing, Y. L.; Que, W. X.; Niu, C. M.; Shao, J. Y. Highly efficient flexible perovskite solar cells using solution-derived NiO_x hole contacts. *ACS Nano* **2016**, *10*, 3630–3636.

[36] Jo, J. W.; Seo, M.-S.; Park, M.; Kim, J.-Y.; Park, J. S.; Han, I. K.; Ahn, H.; Jung, J. W.; Sohn, B.-H.; Ko, M. J. et al. Improving performance and stability of flexible planar-heterojunction perovskite solar cells using polymeric hole-transport material. *Adv. Funct. Mater.* **2016**, *26*, 4464–4471.

[37] Conings, B.; Baeten, L.; Jacobs, T.; Dera, R.; D'Haen, J.; Manca, J.; Boyen, H.-G. An easy-to-fabricate low-temperature TiO_2 electron collection layer for high efficiency planar heterojunction perovskite solar cells. *APL Mater.* **2014**, *2*, 081505.

[38] Zardetto, V.; Di Giacomo, F.; Garcia-Alonso, D.; Keuning, W.; Creatore, M.; Mazzuca, C.; Reale, A.; Di Carlo, A.; Brown, T. M. Fully plastic dye solar cell devices by low-temperature UV-irradiation of both the mesoporous TiO_2 photo- and platinized counter-electrodes. *Adv. Energy Mater.* **2013**, *3*, 1292–1298.

[39] George, S. M. Atomic layer deposition: An overview. *Chem. Rev.* **2010**, *110*, 111–131.

[40] Wu, Y. Z.; Yang, X. D.; Chen, H.; Zhang, K.; Qin, C. J.; Liu, J.; Peng, W. Q.; Islam, A.; Bi, E. B.; Ye, F. et al. Highly compact TiO_2 layer for efficient hole-blocking in perovskite solar cells. *Appl. Phys. Express* **2014**, *7*, 052301.

[41] Katoch, A.; Kim, H.; Hwang, T.; Kim, S. S. Preparation of highly stable TiO_2 sols and nanocrystalline TiO_2 films via a low temperature sol–gel route. *J. Sol-Gel Sci. Technol.* **2012**, *61*, 77–82.

[42] Xiao, M. D.; Huang, F. Z.; Huang, W. C.; Dkhissi, Y.; Zhu, Y.; Etheridge, J.; Gray-Weale, A.; Bach, U.; Cheng, Y.-B.; Spiccia, L. A fast deposition-crystallization procedure for highly efficient lead iodide perovskite thin-film solar cells. *Angew. Chem.* **2014**, *126*, 10056–10061.

[43] Pascoe, A. R.; Yang, M. J.; Kopidakis, N.; Zhu, K.; Reese, M. O.; Rumbles, G.; Fekete, M.; Duffy, N. W.; Cheng, Y.-B. Planar versus mesoscopic perovskite microstructures: The influence of $CH_3NH_3PbI_3$ morphology on charge transport and recombination dynamics. *Nano Energy* **2016**, *22*, 439–452.

[44] Peng, B.; Jungmann, G.; Jäger, C.; Haarer, D.; Schmidt, H.-W.; Thelakkat, M. Systematic investigation of the role of compact TiO_2 layer in solid state dye-sensitized TiO_2 solar cells. *Coord. Chem. Rev.* **2004**, *248*, 1479–1489.

[45] Wang, X. M.; Fang, Y. L.; He, L.; Wang, Q.; Wu, T. Influence of compact TiO_2 layer on the photovoltaic characteristics of the organometal halide perovskite-based solar cells. *Mater. Sci. Semicond. Process.* **2014**, *27*, 569–576.

[46] Fakharuddin, A.; Di Giacomo, F.; Ahmed, I.; Wali, Q.; Brown, T. M.; Jose, R. Role of morphology and crystallinity of nanorod and planar electron transport layers on the performance and long term durability of perovskite solar cells. *J. Power Sources* **2015**, *283*, 61–67.

[47] Fakharuddin, A.; Di Giacomo, F.; Palma, A. L.; Matteocci F.; Ahmed, I.; Razza, S.; D'Epifanio, A.; Licoccia, S.; Ismail, J.; Di Carlo, A. et al. Vertical TiO_2 nanorods as a medium for stable and high-efficiency perovskite solar modules. *ACS Nano* **2015**, *9*, 8420–8429.

[48] Kavan, L.; Tétreault, N.; Moehl, T.; Grätzel, M. Electrochemical characterization of TiO_2 blocking layers for dye-sensitized solar cells. *J. Phys. Chem. C* **2014**, *118*, 16408–16418.

[49] Zaban, A.; Greenshtein, M.; Bisquert, J. Determination of the electron lifetime in nanocrystalline dye solar cells by open-circuit voltage decay measurements. *ChemPhysChem* **2003**, *4*, 859–864.

[50] Sridhar, N.; Freeman, D. A study of dye sensitized solar cells under indoor and low level outdoor lighting: Comparison to organic and inorganic thin film solar cells and methods to address maximum power point tracking. In *Proceedings of the 26th European Photovoltaic Solar Energy Conference and Exhibition (EUPVSEC2011)*, Hamburg, Germany, 2011, pp 232–236.

[51] De Rossi, F.; Brown, T. M.; Pontecorvo, T. Flexible photovoltaics for light harvesting under LED lighting. In *Proceedings of the 15th International Conference on Environment and Electrical Engineering*, Rome, Italy, 2015, pp 2100–2103.

[52] Mathews, I.; King, P. J.; Stafford, F.; Frizzell, R. Performance of III–V solar cells as indoor light energy harvesters. *IEEE J. Photovolt.* **2016**, *6*, 230–235.

[53] Ricoh Company Ltd. Ricoh develops high-performance complete solid-state dye-sensitized solar cell suitable for indoor lighting [Online]. https://www.ricoh.com/release/2014/0611_1.html (accessed May 3, 2016)